



THE UNIVERSITY *of* EDINBURGH

Edinburgh Research Explorer

Molecular multifunctionality preservation upon surface deposition for a chiral single-molecule magnet

Citation for published version:

Mitcov, D, Pedersen, AH, Ceccato, M, Gelardi, RM, Hassenkam, T, Konstantatos, A, Reinholdt, A, Sorensen, MA, Thulstrup, PW, Vinum, MG, Wilhelm, F, Rogalev, A, Wernsdorfer, W, Brechin, EK & Piligkos, S 2019, 'Molecular multifunctionality preservation upon surface deposition for a chiral single-molecule magnet', *Chemical Science*, vol. 10, no. 10, pp. 3065-3073. <https://doi.org/10.1039/C8SC04917C>

Digital Object Identifier (DOI):

[10.1039/C8SC04917C](https://doi.org/10.1039/C8SC04917C)

Link:

[Link to publication record in Edinburgh Research Explorer](#)

Document Version:

Peer reviewed version

Published In:

Chemical Science

General rights

Copyright for the publications made accessible via the Edinburgh Research Explorer is retained by the author(s) and / or other copyright owners and it is a condition of accessing these publications that users recognise and abide by the legal requirements associated with these rights.

Take down policy

The University of Edinburgh has made every reasonable effort to ensure that Edinburgh Research Explorer content complies with UK legislation. If you believe that the public display of this file breaches copyright please contact openaccess@ed.ac.uk providing details, and we will remove access to the work immediately and investigate your claim.



Chemical Science

Accepted Manuscript



This article can be cited before page numbers have been issued, to do this please use: D. Mitcov, A. H. Pedersen, M. Ceccato, R. M. Gelardi, T. Hassenkam, A. Konstantatos, A. Reinholdt, M. A. Sørensen, P. W. W. Thulstrup, M. G. Vinum, F. Wilhelm, A. Rogalev, W. Wernsdorfer, E. K. Brechin and S. Piligkos, *Chem. Sci.*, 2019, DOI: 10.1039/C8SC04917C.



This is an Accepted Manuscript, which has been through the Royal Society of Chemistry peer review process and has been accepted for publication.

Accepted Manuscripts are published online shortly after acceptance, before technical editing, formatting and proof reading. Using this free service, authors can make their results available to the community, in citable form, before we publish the edited article. We will replace this Accepted Manuscript with the edited and formatted Advance Article as soon as it is available.

You can find more information about Accepted Manuscripts in the [author guidelines](#).

Please note that technical editing may introduce minor changes to the text and/or graphics, which may alter content. The journal's standard [Terms & Conditions](#) and the ethical guidelines, outlined in our [author and reviewer resource centre](#), still apply. In no event shall the Royal Society of Chemistry be held responsible for any errors or omissions in this Accepted Manuscript or any consequences arising from the use of any information it contains.

Molecular multifunctionality preservation upon surface deposition for a chiral Single-Molecule Magnet

Dmitri Mitcov,^a Anders H. Pedersen,^a Marcel Ceccato,^a Rikke M. Gelardi,^a Tue Hassenkam,^a Andreas Konstantatos,^a Anders Reinholdt,^a Mikkel A. Sørensen,^a Peter W. Thulstrup,^a Morten G. Vinum,^a Fabrice Wilhelm,^b Andrei Rogalev,^b Wolfgang Wernsdorfer,^{c†} Euan K. Brechin^d and Stergios Piligkos^{*a}

Received 00th January 20xx,
Accepted 00th January 20xx

DOI: 10.1039/x0xx00000x

www.rsc.org/

The synthesis and characterization of a chiral, enneanuclear Mn(III)-based, Single-Molecule Magnet, $[\text{Mn}_9\text{O}_4(\text{Me-sao})_6(\text{L})_3(\text{MeO})_2(\text{MeOH})_3]\text{Cl}$ (**1**; Me-saoH₂ = methylsalicylaldoxime, HL = lipoic acid) is reported. Compound **1** crystallizes in the orthorhombic $P2_12_12_1$ space group and consists of a metallic skeleton describing a defect super-tetrahedron missing one vertex. The chirality of the $[\text{Mn}^{\text{III}}_9]$ core originates from the directional bridging of the Me-sao²⁻ ligands via the –N–O–oximate moieties, which define a clockwise (**1ΔΔ**) or counter-clockwise (**1ΛΛ**) rotation in both the upper $[\text{Mn}^{\text{III}}_3]$ and lower $[\text{Mn}^{\text{III}}_6]$ subunits. Structural integrity and retention of chirality upon dissolution and upon deposition on (a) gold nanoparticles, **1@AuNPs**, (b) transparent Au(111) surfaces, **1ΛΛ@t-Au(111)**; **1ΔΔ@t-Au(111)**, and (c) epitaxial Au(111) on mica surfaces, **1@e-Au(111)**, was confirmed by CD and IR spectroscopies, mass spectrometry, TEM, XPS, XAS, and AFM. Magnetic susceptibility and magnetization measurements demonstrate the simultaneous retention of SMM behaviour and optical activity, from the solid state, *via* dissolution, to the surface deposited species.

Introduction

Modern information technology is based on the combined use of the charge and spin properties of electrons, exploited within devices incorporating magnetic nanomaterials.^{1, 2} The next generation of such devices will incorporate molecular magnetic materials that serve the purpose of miniaturization and allow the exploitation of the quantum properties that matter exhibits at this scale.³ The controlled deposition of such materials on substrates⁴⁻⁷ and the subsequent addressing and manipulation of their magnetic moment at the molecular level⁸⁻¹⁰ is a prerequisite for device realization. This can be achieved through the use of chiral magnetic molecular materials, since the absence of an inversion centre leads to efficient coupling of electric fields to the molecular magnetic moment,¹¹ and to magnetochirality,¹²⁻¹⁴ a second order non-reciprocal effect that can be harnessed by unpolarised light.¹⁴ Thus, surface deposited chiral magnetic molecular materials

are excellent candidates for the realization of spintronic devices operating on the basis of electric or optical control of molecular magnetic moments via spin-electric coupling or the magnetochiral effect. Single-Molecule Magnets^{15, 16} (SMMs) are a class of molecular materials currently considered for applications in molecular spintronics, such as quantum computing.¹⁷⁻¹⁹ The unique potential of SMMs lies in their physics dominated by quantum effects such as quantum tunnelling of the magnetisation,²⁰ Berry phase²¹ and spin coherence.²² However, there still persists a crucial open question: how are the molecular properties affected by the drastic change in molecular environment that occurs upon surface deposition?

Until very recently, the few studies that addressed the spin dynamics of SMMs deposited on metallic surfaces showed serious alteration of the molecular properties after deposition on the surface and failed to observe magnetic hysteresis. It has been shown that Mn₁₂ is reduced when deposited at monolayer level on gold.²³ It has also been shown by several recent studies that the molecular magnetic properties of SMMs evolve upon dissolution^{24, 25} or deposition on surfaces.²⁶ It is only very recently that magnetic hysteresis from a tetranuclear Fe(III) SMM anchored on a gold surface by thiolate groups,²⁷⁻²⁹ or on carbon-nanotubes (CNTs),³⁰ from Mn₁₂ on Au(111),²⁸ and from Ln-based SMMs anchored on CNTs,³¹ on gold,³² on magnesium oxide,³³ or on silicon,³⁴ was detected. The grafting of Cr₇Ni on gold and on highly oriented pyrolytic graphite was also reported.^{35, 36} Very recently, engineering of the magnetic coupling and anisotropy of a Co^{II}-

^a Department of Chemistry, University of Copenhagen, Universitetsparken 5, DK-2100, Copenhagen, Denmark.

^b ESRF - The European Synchrotron, CS 40220, 38043 Grenoble Cedex 9, France.

^c Institute Néel, CNRS, BP 166, 25 Avenue de Martyrs, Grenoble, 38042 Cedex 9, France.

^d EaStCHEM School of Chemistry, The University of Edinburgh, David Brewster Road, Edinburgh, EH9 3FJ, United Kingdom.

† Present Address: Institute of Nanotechnology, Karlsruhe Institut für Technologie, 76344 Eggenstein-Leopoldshafen, Germany.

Electronic Supplementary Information (ESI) available: Full experimental details and additional data for all the characterizations presented in the main text. See DOI: 10.1039/x0xx00000x



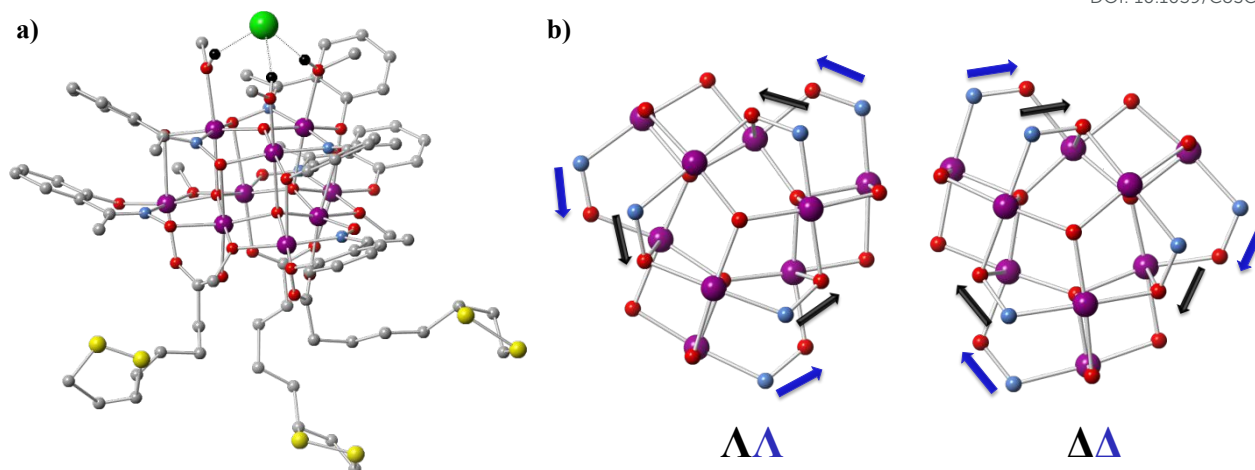


Figure 1. Structure of $[\text{Mn}_9\text{O}_4(\text{Me-sao})_6(\text{L})_3(\text{MeO})_3(\text{MeOH})_3]\text{Cl}$. a) Molecular structure of **1**. Color scheme: Mn - purple, N - blue, O - red, C - gray, S - yellow, Cl - green. Hydrogen atoms have been omitted for clarity, except those of the methanol molecules (black) that form H-bonds with the Cl counter-anion. b) $1\Delta\Delta$ and $1\Lambda\Lambda$ configurations of the $[\text{Mn}^{\text{III}}_9]$ core in **1**.

and of a Ni^{II}-based SMMs with the Fe_3O_4 (111) surface,³⁷ was demonstrated. Recent review articles present the main strategies for the attachment of SMMs on surfaces.⁴⁻⁶ Chiral SMMs have been extensively studied in the bulk³⁸ but to the best of our knowledge simultaneous retention of chirality and SMM behaviour has never been demonstrated upon surface deposition.

Herein, we present the synthesis and characterization of a chiral, enneanuclear Mn(III)-based SMM, $[\text{Mn}_9\text{O}_4(\text{Me-sao})_6(\text{L})_3(\text{MeO})_3(\text{MeOH})_3]\text{Cl}$ (**1**), where LH is lipoic acid and Me-saoH₂ is methylsalicylaldoxime, functionalized for surface deposition and stable in solution. We demonstrate, for the first time, the simultaneous retention of superparamagnetism-like SMM behaviour and chirality, from the solid state, via dissolution, to the surface deposited species.

Results and discussion

Solid state

1 (Figures 1a, S1a) crystallizes in the orthorhombic $P2_12_12_1$ space group (Table S1) which is one of the 65 Sohncke space groups that contain only symmetry operations of the first kind (rotations and translations) and can accommodate chiral molecules.³⁹ Only species of the same enantiomeric structure are present in a given crystal of **1**. The chirality of the $[\text{Mn}^{\text{III}}_9]$ core in **1** originates from the directional bridging of the Me-sao²⁻ ligands via the -N-O- oximate moieties, which define a clockwise ($1\Delta\Delta$) or counter-clockwise ($1\Lambda\Lambda$) rotation in both the upper $[\text{Mn}^{\text{III}}_3]$ and lower $[\text{Mn}^{\text{III}}_6]$ subunits (Figure 1b), with respect to the axis normal to both planes. The metal-core of **1** consists of nine Mn(III) ions describing a defect super-tetrahedron missing one vertex (Figure 1a). In the upper $[\text{Mn}^{\text{III}}_3]$ subunit, the three Mn(III) ions are linked by a central $\mu_3\text{-O}^{2-}$ ion, while the edges of the $[\text{Mn}^{\text{III}}_3]$ triangle consist of three bridging -N-O- oximates (Mn-N-O-Mn torsion angles:

38.0 - 39.5°, Tables S2-S3) from the Me-sao²⁻ ligands. The upper face of the $[\text{Mn}^{\text{III}}_3]$ unit is capped by three MeOH molecules (Mn-O_{MeOH} = 2.180 - 2.206 Å Tables S4-S5) and the counter-anion (Cl⁻) that is H-bonded to the capping solvent (H_{MeOH}...Cl⁻ 2.190 - 2.200 Å). In the basal $[\text{Mn}^{\text{III}}_6]$ subunit, the almost co-planar Mn(III) ions are alternately connected from the exterior by three oximates (Mn-N-O-Mn torsion angles: 8.6 - 13.7°, Tables S2-S3) and three methoxides (Mn-O_{μ-MeO}-Mn angles: 98.79 - 100.16°, Tables S6-S7), while from the interior the metal-ions are linked via three $\mu_4\text{-O}^{2-}$ bridges. Thus, the six Mn(III) ions form a triangle with three ions positioned at the vertices and the other three at the middle of the edges. The lower face of the $[\text{Mn}^{\text{III}}_6]$ subunit is capped by three sulfur-containing carboxylates, bonding in a bidentate bridging fashion conferring tripodal ligand attributes to **1**. The inner $\mu_4\text{-O}^{2-}$ ion from the basal $[\text{Mn}^{\text{III}}_6]$ unit, the oximate O-atoms from the bridging aldoximes, the phenoxide O-atoms of Me-sao²⁻ and the -N-O- oximate bridges from the upper $[\text{Mn}^{\text{III}}_3]$ subunit link $[\text{Mn}^{\text{III}}_3]$ and $[\text{Mn}^{\text{III}}_6]$ to form the $[\text{Mn}^{\text{III}}_9]$ defect super-tetrahedron. The Jahn-Teller axes of the Mn(III) ions are perpendicular to both the $[\text{Mn}^{\text{III}}_3]$ and $[\text{Mn}^{\text{III}}_6]$ planes and are approximately co-parallel to each other (Figure S1). The crystal packing and intermolecular interactions are shown in Figures S2-S4.

Direct-current (d.c.) magnetic susceptibility studies in a magnetic field, B , of 0.1 T, were performed on polycrystalline **1**, the purity of which was confirmed by powder X-ray diffraction (Figure S5). The χT versus T data, where $\chi = M / B$, with M the magnetization, χ the molar magnetic susceptibility and T the temperature, are shown in Figure 2. The χT product of **1** at 270 K is 23.2 cm³·K·mol⁻¹, lower than that expected for the spin-only contributions of nine uncorrelated Mn(III) ions (27 cm³·K·mol⁻¹, $S_{\text{Mn}} = 2$, $g_{\text{Mn}} = 2$). Upon cooling, the χT product decreases to reach 16.7 cm³·K·mol⁻¹ at 50 K, indicative of dominant antiferromagnetic interactions in **1**. Below 50 K, the χT product increases to 19.5 cm³·K·mol⁻¹ at 10 K. Upon further



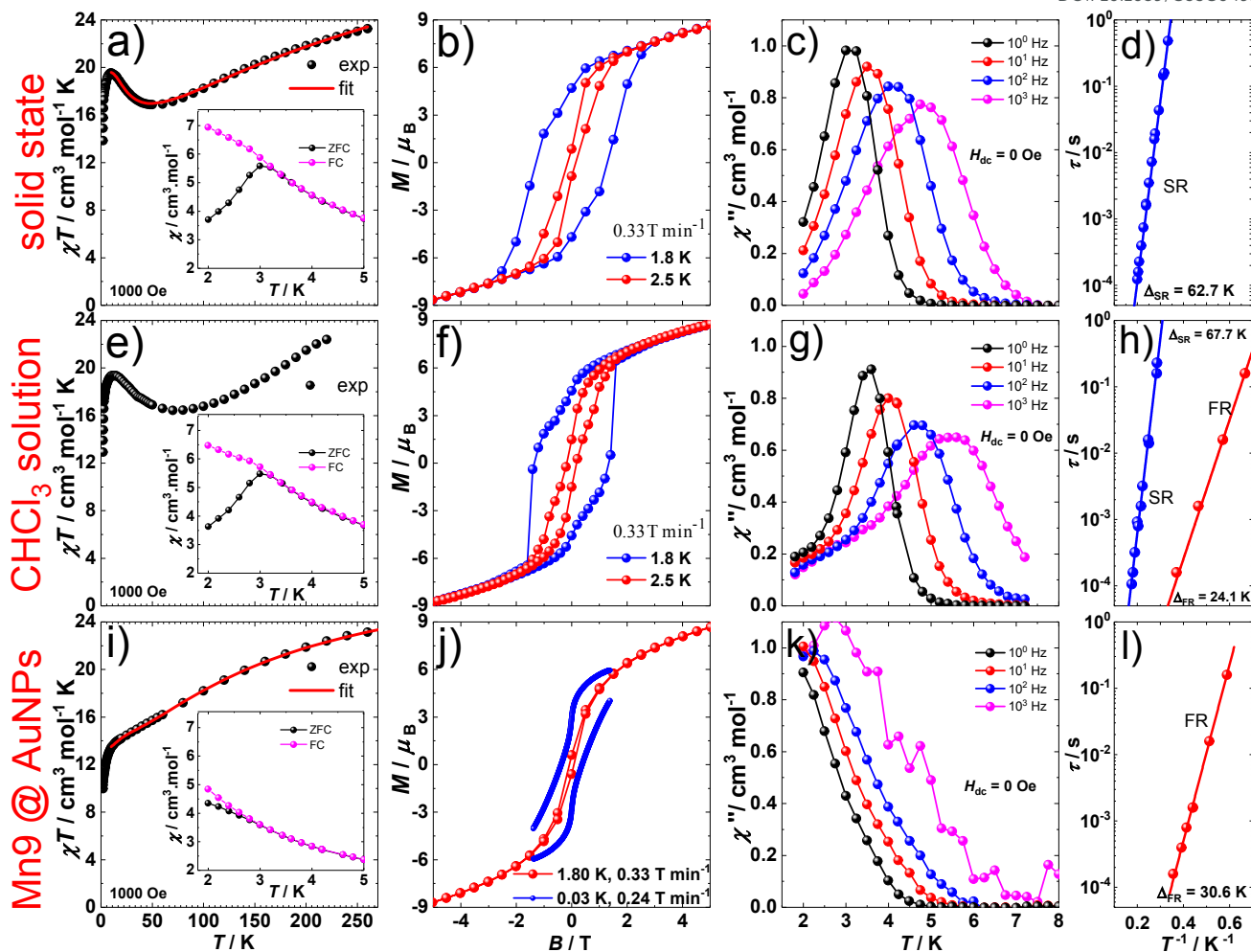


Figure 2. Magnetic properties of $[\text{Mn}_9\text{O}_4(\text{Me-sao})(\text{L})_3(\text{MeO})_2(\text{MeOH})_2]\text{Cl}$. Solid state (a, b, c, d), 19.6 mM CHCl_3 solution (e, f, g, h) and on AuNPs (i, j, k, l). a, e, i, χT versus T plots at 0.1 T, with $\chi = M/B$ the molar magnetic susceptibility of **1**, inset: ZFC and FC susceptibility measurements in an applied $d.c.$ field of 0.1 T; b, f, j, $d.c.$ magnetization hysteresis loops at 1.8 and 2.5 K and 0.33 T min^{-1} (b, f) and at 1.8 K and 0.33 T min^{-1} and at 0.03 K and 0.24 T min^{-1} (j); c, g, k, out-of-phase, χ'' , component of the $a.c.$ susceptibility at 10^0 , 10^1 , 10^2 and 10^3 Hz at $T < 8$ K, in a 3.5 Oe $a.c.$ field and in zero $d.c.$ field. Solid lines are guides for the eye; d, h, l, Arrhenius τ vs T^{-1} plot in zero $d.c.$ field for the fast-relaxing (FR) and slow-relaxing (SR) species. The solid lines represent the best fit to the Arrhenius law of the frequency and temperature dependent χ'' data.

cooling, χT decreases rapidly to $13.6 \text{ cm}^3 \cdot \text{K} \cdot \text{mol}^{-1}$, most likely because of the anisotropy of Mn(III) ions. The nesting and the absence of magnetization saturation in the reduced magnetisation curves for polycrystalline **1** (Figure S20), confirms its magnetic anisotropy. A bifurcation between the zero-field-cooled (ZFC) and field-cooled (FC) susceptibilities (Figure 2) indicates a blocking temperature, T_B , of 3 K. Below T_B , magnetic hysteresis (coercive field of 1.3 T at 1.8 K and 0.33 T min^{-1}) is observed (Figure 2), which is the experimental manifestation of SMM (superparamagnetic-like) behavior.

Modeling of the static magnetic properties of **1** on the basis of a spin-Hamiltonian is far from straightforward because of the large dimension ($5^9 = 1953125$) of the associated spin-Hamiltonian matrix. Within an isotropic model, use of Irreducible Tensor Operator (ITO) algebra⁴⁰ allows blocking of the spin-Hamiltonian matrix into nineteen blocks (SI §6.2), each corresponding to a given value of the total spin, S . Thus, the 180325 S multiplets of **1** (Table S8), with S varying between

0 and 18, were grouped in to nineteen blocks of dimensions ranging from 1 ($S = 18$) to 25200 ($S = 4$). These were subsequently numerically diagonalized by use of standard techniques.⁴¹ The temperature dependence of the χT product of **1** was numerically fitted, down to 10 K, to an isotropic spin-Hamiltonian model by use of the Levenberg-Marquardt algorithm.⁴² To avoid overparameterization, we considered the simplest model of magnetic exchange in **1** (SI §6.2), where J_1 , J_2 and J_3 are the isotropic exchange parameters within $[\text{Mn}^{\text{III}}_6]$, $[\text{Mn}^{\text{III}}_3]$ and between $[\text{Mn}^{\text{III}}_6]$ and $[\text{Mn}^{\text{III}}_3]$, respectively (Figure S32). This resulted in the best fit parameters: $J_1 = -7.6 \text{ cm}^{-1}$, $J_2 = 1.8 \text{ cm}^{-1}$ and $J_3 = -1.6 \text{ cm}^{-1}$ (in the $-2J$ convention). These results are in excellent agreement with previous magnetostructural correlations developed for similar oxime-bridged Mn(III)-based SMMs, where Mn–N–O–Mn torsion angles above or below 31° lead to ferromagnetic ($J > 0$) or antiferromagnetic ($J < 0$) interactions, respectively.^{43, 44} Within this highly symmetric isotropic model, the ground spin state of **1** is a doubly



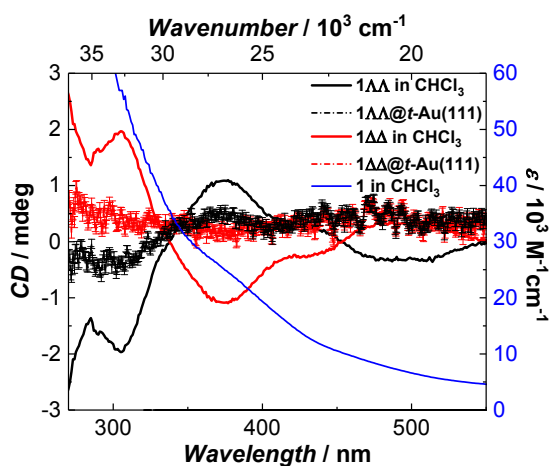


Figure 3. Room temperature absorption spectrum of **1** (blue) and Circular Dichroism spectra of **1ΔΔ** (red) and **1ΔΔ** (black) in CHCl_3 (background corrected data, See SI) and as monolayers on Au(111) (raw data). The intensity of **1ΔΔ@t-Au(111)** and **1ΔΔ@t-Au(111)** was multiplied by a factor of 10 to increase its visibility.

degenerate $S = 5$ with numerous excited multiplets lying very low in energy (Figure S33a). However, given the magnetically anisotropic nature of Mn(III), description of the low temperature magnetic properties of **1** in terms of S multiplets is meaningless, since the anisotropy-induced splitting of the m_s sublevels of these S -multiplets is much larger (Figure S35, Table S9) than the isotropic exchange induced splitting between S -multiplets (Figure S33a). Use of an iterative subspace approach, known as the Davidson algorithm,^{45, 46} that exploits the sparse nature of the spin-Hamiltonian matrix,^{47, 48} allowed exact determination of the 32 lowest lying eigenvalues and eigenvectors (SI §6.2). This subspace was subsequently used to model the low temperature magnetic properties of **1** (Figure S34) allowing estimation of the single-ion uniaxial anisotropy of Mn(III), $D_{\text{Mn}} = -3.4 \text{ cm}^{-1}$.

The spin-dynamics of **1** were probed by *alternating current* (a.c.) magnetic susceptibility measurements, revealing frequency and temperature dependent in-phase (χ') and out-of-phase (χ'') components (Figure 2 and S21-S22). These were used to extract the energy barrier of the thermally activated process, Δ_{eff} , by fitting the relaxation time, τ , to the Arrhenius law $\tau = \tau_0 \exp(\Delta_{\text{eff}}/k_B T)$, with k_B the Boltzmann constant and τ_0 a pre-exponential factor, resulting in: $\Delta_{\text{eff}}/k_B = 62.7 \text{ K}$ and $\tau_0 = 4.0 \cdot 10^{-10} \text{ s}$.

Solution

Since single crystals of **1** are very dark, preventing solid state optical activity measurements, we performed these on chloroform solutions of individual single-crystals of **1**. Circular Dichroism (CD) spectra showed mirror-image Cotton effects at several wavelengths (Figure 3). The higher intensity bands below 330 nm are attributed to charge-transfer²⁵ (CT) and/or internal ligand transitions⁴⁹ (Figure S19). The weaker bands observed above 330 nm are attributed to the seven possible $d-d$ transitions for Mn(III) in a low-symmetry crystal field²⁵. The solution CD spectra of the enantiomers of **1** show that it does not racemize or decompose in solution. Further evidence of

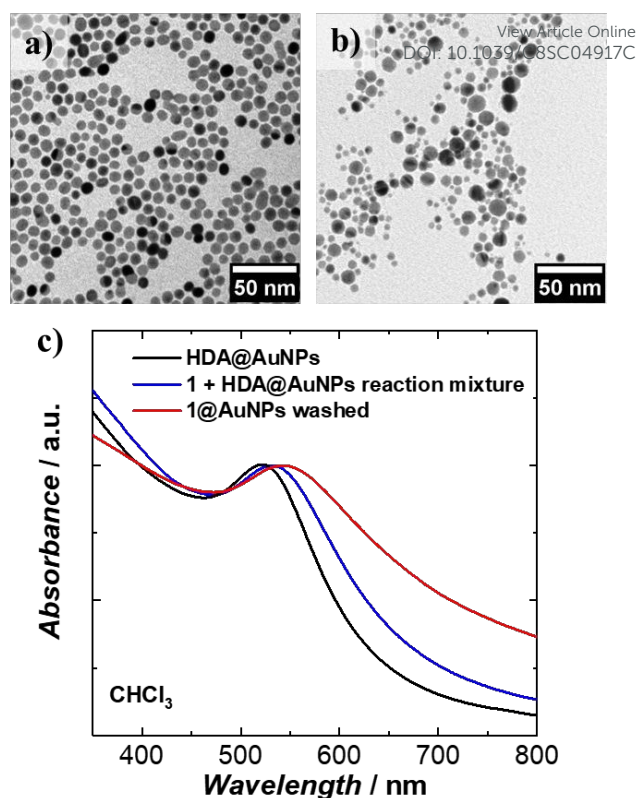


Figure 4. Transmission Electron Microscopy (TEM) images of a) **HDA@AuNPs** and b) evenly distributed **1@AuNPs** formed after the deposition of **1** on AuNPs; c) Plasmon resonance spectra of **HDA@AuNPs** and **1@AuNPs**.

the stability of **1** in solution was obtained by infrared (IR) spectroscopy (Figure S6) and mass spectrometry (Figure S7). *D.c.* magnetization measurements on 19.6 mM chloroform solutions of **1** revealed very similar behavior to that observed in the solid state (Figure 2). The temperature dependence of the χT product, T_B , and the magnetic hysteresis of the frozen solution of **1** are very similar to the analogous measurements in the solid state (Figure 2), reflecting the structural integrity of **1** in solution. A.c. susceptibility measurements on 19.6 mM chloroform solutions (Figures 2 and S23-S24) showed the presence of a slow-relaxing (SR) and a fast-relaxing (FR) process. Since the molecular spin-dynamics are extremely sensitive to the coordination sphere of the metal centres,^{50, 51} these are attributed to a SR and a FR species, for which we obtain: Δ_{eff}/k_B of 66.7 and 24.1 K and $\tau_0 = 8.2 \cdot 10^{-10}$ and $1.6 \cdot 10^{-8} \text{ s}$, respectively. Magnetization measurements on a 6.8 mM chloroform solution of **1** showed an increase in the FR species (Figures S25-S26). This observation suggests the loss of terminal MeOH ligands upon dissolution, leading to the modification of the axial anisotropy of Mn(III) centres and/or to a change in the Mn(III) Jahn-Teller axis orientation at these centres.^{52, 53}

Surface deposition

1 was chemically grafted on several metallic gold substrates by exploiting the high affinity of sulfur for gold^{54, 55} (40–50 kcal mol⁻¹, close to the Au–Au bond) and the tripodal ligand nature



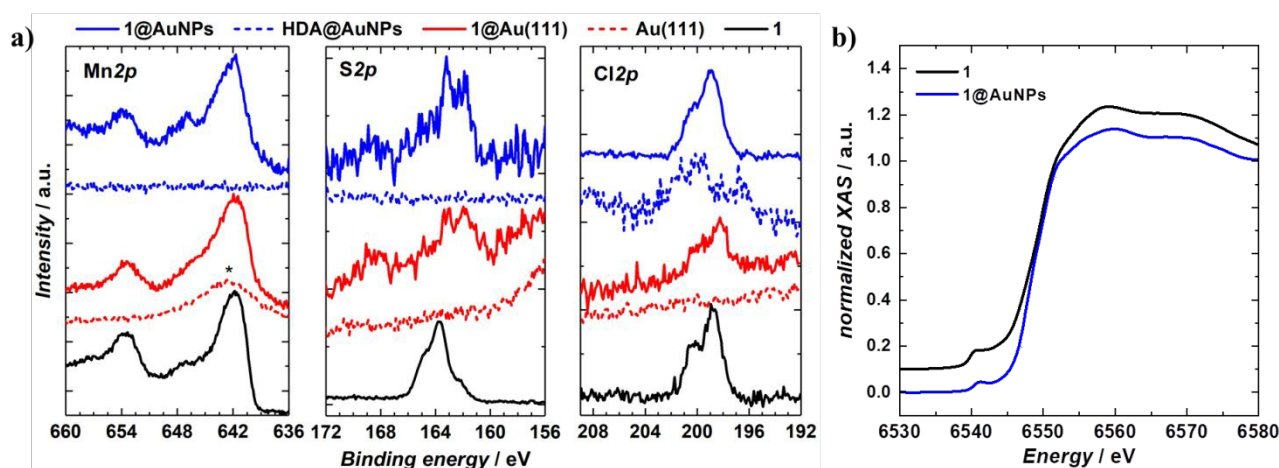


Figure 5. XPS and XAS spectra of bulk and surface deposited $[\text{Mn}_3\text{O}_4(\text{Me-sao})_6(\text{L})_2(\text{MeO})_3(\text{MeOH})_3]\text{Cl}$. A) XPS spectra of **1**, **1@AuNPs**, **1@Au(111)**, **HDA@AuNPs**, and blank **Au(111)** surface at $\text{Mn}2p$, $\text{S}2p$ and $\text{Cl}2p$ core levels. The $\text{Mn}2p_{3/2}$ core level line in **1@Au(111)** is superimposed on the $\text{Au}4p_{3/2}$ feature, marked with *; b) Normalised XAS spectra of **1** and **1@AuNPs**, the intensity of the former is shifted by 0.1 a.u. for clarity of presentation.

of **1**. These were: a) gold nanoparticles, **AuNPs**, used to increase the specific surface area of the substrate for the study of the magnetic properties of grafted **1** (**1@AuNPs**) by conventional magnetometry;⁵⁶ b) transparent $\text{Au}(111)$ surface,⁵⁷ $\text{t-Au}(111)$, to allow probing of the optical activity of grafted **1** (**1@Au(111)** and **1@Au(111)**, respectively); and c) epitaxial $\text{Au}(111)$ surface, **e-Au(111)**, to study the organization of **1** on this substrate (**1@e-Au(111)**).

1@AuNPs were obtained from hexadecylamine (HDA) capped **AuNPs** (**HDA@AuNPs**) of 7.3 nm average size, as determined by Transmission Electron Microscopy (TEM, Figures 4 and S8-S9). Taking into account some simple geometric calculations,⁵⁶ a 10% by weight ratio of **1** is necessary to achieve full coverage. Upon grafting, the dark red color of **HDA@AuNPs** changed to red-violet for **1@AuNPs** (plasmon resonances at 522 and 542 nm, respectively, Figure 4), indicating a change of dielectric constant around the **AuNPs**.⁵⁸ To confirm grafting of **1** on **AuNPs** rather than adsorption, X-ray Photoelectron Spectroscopy (XPS) measurements of **1**, **HDA@AuNPs** and **1@AuNPs** were carried out on the $\text{Au}4f$, $\text{Au}4p$, $\text{Mn}3s$, $\text{Mn}2p$, $\text{S}2p$, $\text{Cl}2p$, $\text{N}1s$, $\text{O}1s$ and $\text{C}1s$ regions of binding energies (Figures 5a, S10-S12 and Tables S8-S10). The photoemission of **1@AuNPs** allowed confirmation of the presence of Mn, S, and Cl. These elements are not present or have different binding energies in **HDA@AuNPs** when compared to **1**. The $\text{S}2p$ region is particularly interesting because $\text{S}2p_{3/2}$ peaks at 161.8-161.9 eV are assigned to thiols bound to the Au surface while $\text{S}2p_{3/2}$ peaks at 163.2-163.5 eV are consistent with unbound thiols/disulfides.⁵⁹ The observed shift of the $\text{S}2p_{3/2}$ bands from 163.5 eV (**1**) to 161.9 eV (**1@AuNPs**) of binding energy (and of the less intense $\text{S}2p_{1/2}$ bands from 164.7 eV (**1**) to 162.8 eV (**1@AuNPs**)) and the change of their intensity profile (Figures 5a and S11) shows that sulfur is reduced upon binding to Au,⁵⁹ confirming grafting of **1**. Information on the surface stoichiometry (Tables S8-S9) was derived by quantitative analysis of the XPS spectra. The stability of **1** upon deposition

on **AuNPs** can be confirmed by the Mn/S ratio values since these elements are not present in **HDA@AuNPs**. The measured Mn/S ratio in **1** and in **1@AuNPs** fits well with the expected stoichiometric value (Table S9), whereas S/N, Mn/N, and S/Cl ratios are lower than the expected ones in **1@AuNPs** suggesting that elements such as N and Cl are present in excess likely due to their high content on the surface of **HDA@AuNPs** used as starting material in the preparation of **1@AuNPs**. Mn(III)-based SMMs often undergo reduction to Mn(II)-containing species upon deposition on gold.⁶¹ The XPS-derived modified Auger parameter (Table S11), insensitive to charging of non-conducting specimens, has the same value (within standard deviation) for **1**, **1@AuNPs** and **1@Au(111)**, suggesting a constant oxidation state in the three samples.^{62, 63} However, since in XPS, intense $\text{Au}4f$ peaks totally cover the $\text{Mn}3s$ signals, and $\text{Au}4p$ partially interferes with the weak $\text{Mn}2p$ signals (Figure S12), we performed X-ray absorption spectroscopy (XAS) to compare the oxidation state of Mn in **1** and in **1@AuNPs**. The experimental X-ray absorption spectra (Figure 5b) are dominated by the 1s to 4p transitions with a much weaker pre-edge feature, assigned to dipole-forbidden 1s to 3d transitions. This energetically low-lying pre-edge feature, being weakly dependent on the exact ligand field, is usually taken as a fingerprint of the oxidation state of a transition metal. The Mn K-edge spectra of **1** and of **1@AuNPs** reveal a remarkable similarity, confirming that Mn is in the same oxidation state in both systems. By comparison to published Mn(III) K-edge absorption spectra,^{64, 65} we can conclude that the oxidation state of Mn in **1** and **1@AuNPs** is 3+. Furthermore, both **1** and **1@AuNPs** display very weak X-ray Magnetic Circular Dichroism (XMCD) at the Mn K-edge (Figure S13). At the K-edge of a transition metal ion, the XMCD signal is due to the orbital magnetization of the 4p- and 3d-states, induced by the intra-atomic spin-orbit interaction. The XMCD spectrum of **1** (Figure S13) reveals several clear features in the pre-edge, at the edge and also characteristic super-



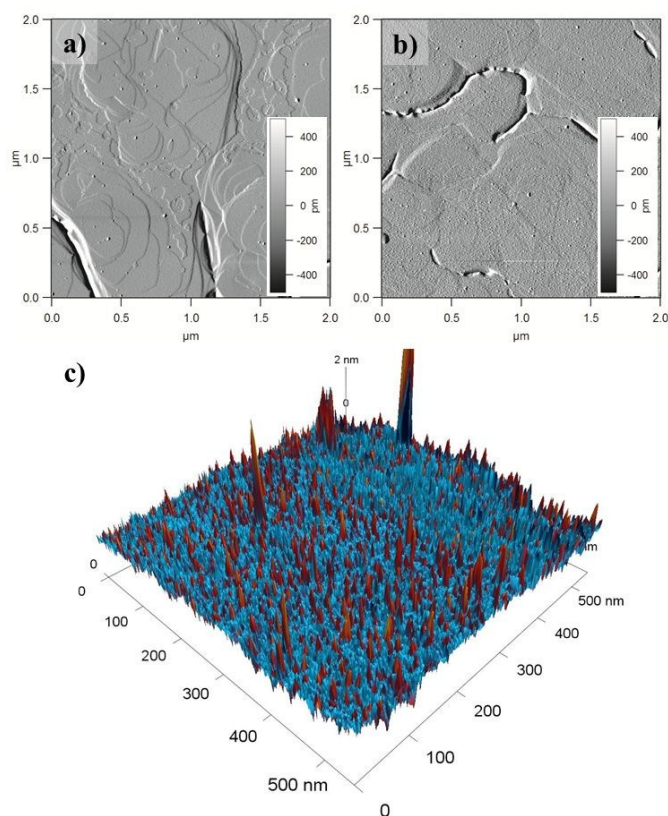


Figure 6. AFM amplitude mode images of a) **e-Au(111)** clean surface with visible atomic steps and b) **1@e-Au(111)**. c) 3D combined phase and height AFM tapping-mode profiles of **1@e-Au(111)**. Red and blue tapping-mode phases correspond to different compressibilities of the deposited material. Individual protrusions coincide with the red phase.

Coster-Kronig multi-electron excitations at ~ 47 eV above the edge.⁶⁶ However, the amplitude of the XMCD signal of **1** is found to be nearly 100 times weaker than the one detected in paramagnetic Mn^{3+} ions in GaN.⁶⁷ This observation indicates significant quenching of orbital moments in **1**.

1@AuNPs, **HDA@AuNPs** and **HL@AuNPs** were investigated in the solid state with SQUID magnetometry. AuNPs are known to display magnetic properties ranging from diamagnetism, through paramagnetism, to ferromagnetism, depending on the type of surface ligand and the degree of coverage.^{68–75} The χT product of **1@AuNPs** at 270 K is $22.2 \text{ cm}^3 \cdot \text{K} \cdot \text{mol}^{-1}$, slightly lower than the $23.2 \text{ cm}^3 \cdot \text{K} \cdot \text{mol}^{-1}$ seen for **1** (Figure 2). Between 270 and 60 K the χT product decreases to a value of $15.7 \text{ cm}^3 \cdot \text{K} \cdot \text{mol}^{-1}$, following the trend observed in **1**. On further cooling, the χT product for **1@AuNPs** continues to decrease, contrary to **1**, until it reaches a plateau around $18.5 \text{ cm}^3 \cdot \text{K} \cdot \text{mol}^{-1}$ between 25 and 10 K. Below 10 K, χT abruptly decreases, as in **1**, to $9.6 \text{ cm}^3 \cdot \text{K} \cdot \text{mol}^{-1}$ at 1.8 K. Fitting of the temperature dependence of the χT product for **1@AuNPs** to the same spin-Hamiltonian model as for **1**, resulted in the best-fit parameters: $J_1 = -4.5 \text{ cm}^{-1}$, $J_2 = 2.7 \text{ cm}^{-1}$ and $J_3 = -2.8 \text{ cm}^{-1}$. Thus, the absence of a maximum in the χT product of **1@AuNPs** at 10 K is mainly due to the modification of the magnetic exchange interactions within the $[\text{Mn}_6]$ subunit (J_1) as a consequence of the distortion of the $[\text{Mn}_9]$ core upon grafting

to the **AuNPs** surface via the sulfur-containing carboxylates bound to the $[\text{Mn}_6]$ subunit. This modification could be assigned to Mn-N-O-Mn torsion angles within the $[\text{Mn}_6]$ subunit evolving from 7.9 – 13.3° (Tables S2–S3), corresponding to $J_1 = -7.6 \text{ cm}^{-1}$, towards the 31° limit.^{43, 44} In fact, a previously reported $[\text{Mn}_9]$ complex presenting a very similar temperature dependence of the χT product to **1@AuNPs** displayed Mn-N-O-Mn torsion angles of 25° within the $[\text{Mn}_6]$ subunit.⁶⁵ The reduced magnetization curves show no saturation and are not superimposable (Figure S20), again confirming the magnetically anisotropic nature of **1@AuNPs**. The magnetization of **1@AuNPs** at 1.8 K and at 5 T is $8.7 \mu_B$, similar to the solid state. A less well pronounced bifurcation between the ZFC and FC susceptibility curves was observed at 3 K for **1@AuNPs** (Figure 2). **1@AuNPs** exhibits magnetic hysteresis (Figure 2 and S29) with a coercive field of 0.08 T at 1.8 K and 0.33 T min^{-1} and of 0.38 T at 0.03 K and 0.24 T min^{-1} . The magnetization observed at low temperatures for **1@AuNPs** was several orders of magnitude higher than for **HDA@AuNPs** or **HL@AuNPs** (Figures S28–S29). Temperature and frequency dependent χ' and χ'' components of the *a.c.* susceptibility were observed (Figures 2 and S27) at zero *d.c.* field from where $\Delta_{\text{eff}}/k_B = 30.6 \text{ K}$ and $\tau_0 = 2.4 \cdot 10^{-9} \text{ s}$ were determined. **HDA@AuNPs** and **HL@AuNPs** displayed no such features (Figures S28–S30). The values of Δ_{eff} , T_B , and of the coercive field for **1@AuNPs** point towards grafting of the FR species on **AuNPs**. This is due to the loss of MeOH, and the possible ensuing reorientation of the Jahn-Teller axis, caused by the multiple washing cycles during the surface deposition of **1**.

Monolayers of **1@e-Au(111)**, **1@t-Au(111)**, **1 Λ @t-Au(111)** and **1 Δ @t-Au(111)**, hereafter collectively referred to as **1@Au(111)**, were prepared by soaking **e-Au(111)** or **t-Au(111)** films in 2 mM solutions of **1**, **1 Λ** or **1 Δ** in chloroform, followed by extensive washing with chloroform. All monolayers were characterised by XPS. The observed binding energies and lineshapes of equivalent XPS bands are the same for **1@AuNPs** and **1@Au(111)** (Figures 5 and S10–S12), confirming the redox integrity of **1** and its grafting to form a monolayer. Stoichiometric analysis of the XPS spectra (Table S8) showed that the Mn/S and Mn/N ratios measured for **1@Au(111)** (Table S19) are higher than the corresponding values for **1** or **1@AuNPs**, suggesting a higher Mn content. The observed excess could be caused by the intense Au4*f* peaks totally superposing the Mn3*s* signals and Au4*p* partially interfering with the weak Mn2*p* signals (Figures 5a and S12). The measured value for the S/N ratio is in good agreement with the value measured in **1**. Since S and N were not detected on the clean Au(111) surface, the value of S/N ratio for **1@Au(111)** can be considered an indirect indication of the $[\text{Mn}_9]$ stability during the deposition process.

Surface coverage was imaged by Atomic Force Microscopy (AFM) of **1@e-Au(111)** (Figures 6 and S14–S16). Comparison of the pristine Au(111) surface (Figure 6a) with this of **1@e-Au(111)** (Figure 6b) shows monolayer coverage of the Au(111) facets with isolated protrusions being distributed across the surface. The heights of these individual protrusions range from 0.5 to 1.1 nm, with an average of 0.7 nm (Figure S16). This



length distribution corresponds well to the length distribution obtained by considering a model where the three sulfur-containing carboxylate bridging ligands either “stand fully elongated” on the Au surface or “lie flat” on it (Figure S17). Such a distribution of topologies would create a difference of compressibility in the deposited monolayer since the [Mn₉] metal core is less compressible than the sulfur-containing carboxylates standing fully elongated on the Au(111) surface. This is confirmed by the phase of the AFM tapping-mode image (color mapping in Figure 6c) where individual protrusions also correspond to a change in the AFM phase. A more detailed insight over the organization of the molecules of **1** on the Au(111) surface, though could be offered by high resolution and low temperature scanning tunneling microscopy combined with angle dependent X-ray Magneto-Circular and/or Linear Dichroisms.^{34, 76}

CD spectra of monolayers of **1Λ@t-Au(111)** and **1ΔΔ@t-Au(111)** showed mirror-image Cotton effects below 450 nm (Figure 3 and S19) corresponding to *d-d* and CT bands in **1**, in very close agreement to the CD spectra observed for solutions of single crystals of **1**. These observations confirm both the deposition of enantiopure **1** on Au(111) and the structural stability of **1** upon surface deposition from solution. The structural integrity of **1** upon deposition on **t-Au(111)** was also confirmed with ATR FT-IR. The obtained IR spectrum of **1@t-Au(111)** is superimposable on that of crystalline **1** (Figure S18) in the 2000 – 650 cm⁻¹ spectral region, with no stretching vibrations specific to the free ligands (Me-saoH₂ or HL, Figure S6).

Conclusions

We have demonstrated that, by exploiting the power of synthetic chemistry and by taking advantage of the chemical affinity of sulfur for gold, we were able to deposit a chiral SMM on a metallic surface, preserving its molecular multifunctionality (superparamagnetism-like behaviour and optical activity) from the solid state, via dissolution, to the surface deposited species. The observed magnetic properties of the enneannucler Mn(III)-based SMM are explained qualitatively on the basis of established magnetostructural correlations, and quantitatively within the spin-Hamiltonian formalism by use of ITO algebra and of an iterative subspace approach, known as the Davidson algorithm. Future efforts will focus on addressing these surface-deposited chiral SMMs by electric fields via spin-electric coupling, and by light via the magnetochiral effect. This will pave the way for the integration of molecular magnetic chiral materials in molecular quantum spintronics devices, the use of which will revolutionize the way we perceive and manipulate information.

Conflicts of interest

There are no conflicts to declare.

Acknowledgements

View Article Online
DOI: 10.1039/C8SC04917C

SP thanks VILLUM FONDEN for research grant 13376. EKB thanks the EPSRC ([EP/P025986/1](#) and [EP/N01331X/1](#)) for funding. WW acknowledges ERC Advanced Grant Moquos No. 741276. The European Synchrotron Radiation Facility is acknowledged for measurements (CH-5014) on beamline ID12.

Notes and references

Crystallographic data (including structure factors) for **1ΔΔ** and **1ΛΛ** have been deposited with the Cambridge Crystallographic Data Centre (CCDC 1839660-1839661). Copies of the data can be obtained, free of charge, on application to Cambridge Crystallographic Data Centre, 12 Union Road, Cambridge CB2 1EZ, UK, (fax: +44-(0)1223-336033 or email: deposit@ccdc.cam.ac.uk).

1. C. Chappert, A. Fert and F. N. Van Dau, *Nat. Mater.*, 2007, **6**, 813-823.
2. A. R. Rocha, V. M. Garcia-Suarez, S. W. Bailey, C. J. Lambert, J. Ferrer and S. Sanvito, *Nat. Mater.*, 2005, **4**, 335-339.
3. L. Bogani and W. Wernsdorfer, *Nat. Mater.*, 2008, **7**, 179-186.
4. A. Cornia, M. Mannini, P. Sainctavit and R. Sessoli, *Chem. Soc. Rev.*, 2011, **40**, 3076-3091.
5. A. Cornia and M. Mannini, in *Molecular Nanomagnets and Related Phenomena*, ed. S. Gao, Springer Berlin Heidelberg, Berlin, Heidelberg, 2015, pp. 293-330.
6. A. Cornia and M. Mannini, *Single-Molecule Magnets on Surfaces*, Springer-Verlag, Berlin Heidelberg, 2014.
7. A. Cornia, D. R. Talham and M. Affronte, in *Molecular Magnetic Materials: Concepts and Applications*, eds. B. Sieklucka and D. Pinkowicz, Wiley - VCH Verlag GmbH & Co. KGaA, 2016, pp. 187-229.
8. S. Thiele, F. Balestro, R. Ballou, S. Klyatskaya, M. Ruben and W. Wernsdorfer, *Science*, 2014, **344**, 1135-1138.
9. M. Urdampilleta, S. Klyatskaya, J. P. Cleuziou, M. Ruben and W. Wernsdorfer, *Nat. Mater.*, 2011, **10**, 502-506.
10. R. Vincent, S. Klyatskaya, M. Ruben, W. Wernsdorfer and F. Balestro, *Nature*, 2012, **488**, 357-360.
11. M. Trif, F. Troiani, D. Stepanenko and D. Loss, *Phys. Rev. Lett.*, 2008, **101**.
12. G. L. J. A. Rikken and E. Raupach, *Nature*, 1997, **390**, 493-494.
13. C. Train, R. Gheorghe, V. Krstic, L. M. Chamoreau, N. S. Ovanesyan, G. L. J. A. Rikken, M. Gruselle and M. Verdaguer, *Nat. Mater.*, 2008, **7**, 729-734.
14. R. Sessoli, M. E. Boulon, A. Caneschi, M. Mannini, L. Poggini, F. Wilhelm and A. Rogalev, *Nat. Phys.*, 2015, **11**, 69-74.
15. D. Gatteschi, R. Sessoli and J. Villain, *Molecular Nanomagnets*, Oxford University Press, New York, 2007.
16. C. A. P. Goodwin, F. Ortu, D. Reta, N. F. Chilton and D. P. Mills, *Nature*, 2017, **548**, 439-442.
17. M. N. Leuenberger and D. Loss, *Nature*, 2001, **410**, 789-793.
18. F. Meier, J. Levy and D. Loss, *Phys. Rev. Lett.*, 2003, **90**.
19. F. Troiani, A. Ghirri, M. Affronte, S. Carretta, P. Santini, G. Amoretti, S. Piligkos, G. Timco and R. E. P. Winpenny, *Phys. Rev. Lett.*, 2005, **94**.



20. L. Thomas, F. Lioni, R. Ballou, D. Gatteschi, R. Sessoli and B. Barbara, *Nature*, 1996, **383**, 145-147.
21. W. Wernsdorfer and R. Sessoli, *Science*, 1999, **284**, 133-135.
22. K. Bader, D. Dengler, S. Lenz, B. Endeward, S. D. Jiang, P. Neugebauer and J. van Slageren, *Nat. Commun.*, 2014, **5**.
23. M. Mannini, P. Sainctavit, R. Sessoli, C. C. D. Moulin, F. Pineider, M. A. Arrio, A. Cornia and D. Gatteschi, *Chem.Eur. J.*, 2008, **14**, 7530-7535.
24. R. Inglis, J. Bendix, T. Brock-Nannestad, H. Weihe, E. K. Brechin and S. Piligkos, *Chem. Sci.*, 2010, **1**, 631-636.
25. J. M. Bradley, A. J. Thomson, R. Inglis, C. J. Milios, E. K. Brechin and S. Piligkos, *Dalton Trans.*, 2010, **39**, 9904-9911.
26. L. Bogani, L. Cavigli, M. Gurioli, R. L. Novak, M. Mannini, A. Caneschi, F. Pineider, R. Sessoli, M. Clemente-Leon, E. Coronado, A. Cornia and D. Gatteschi, *Adv. Mater. (Weinheim, Ger.)*, 2007, **19**, 3906-+.
27. M. Mannini, F. Pineider, P. Sainctavit, C. Danieli, E. Otero, C. Sciancalepore, A. M. Talarico, M. A. Arrio, A. Cornia, D. Gatteschi and R. Sessoli, *Nat. Mater.*, 2009, **8**, 194-197.
28. M. Mannini, F. Pineider, P. Sainctavit, L. Joly, A. Fraile-Rodriguez, M. A. Arrio, C. C. D. Moulin, W. Wernsdorfer, A. Cornia, D. Gatteschi and R. Sessoli, *Adv. Mater. (Weinheim, Ger.)*, 2009, **21**, 167-+.
29. M. Mannini, F. Pineider, C. Danieli, F. Totti, L. Sorace, P. Sainctavit, M. A. Arrio, E. Otero, L. Joly, J. C. Cezar, A. Cornia and R. Sessoli, *Nature*, 2010, **468**, 417-421.
30. L. Bogani, C. Danieli, E. Biavardi, N. Bendiab, A. L. Barra, E. Dalcanale, W. Wernsdorfer and A. Cornia, *Angew. Chem., Int. Ed.*, 2009, **48**, 746-750.
31. S. Kyatskaya, J. R. Galan-Mascaros, L. Bogani, F. Hennrich, M. Kappes, W. Wernsdorfer and M. Ruben, *J. Am. Chem. Soc.*, 2009, **131**, 15143-15151.
32. A. Hofmann, Z. Salman, M. Mannini, A. Amato, L. Malavolti, E. Morenzoni, T. Prokscha, R. Sessoli and A. Suter, *ACS Nano*, 2012, **6**, 8390-8396.
33. C. Wackerlin, F. Donati, A. Singha, R. Baltic, S. Rusponi, K. Diller, F. Patthey, M. Pivetta, Y. Lan, S. Klyatskaya, M. Ruben, H. Brune and J. Dreiser, *Adv. Mater. (Weinheim, Ger.)*, 2016, **28**, 5142-5142.
34. M. Mannini, F. Bertani, C. Tudisco, L. Malavolti, L. Poggini, K. Misztal, D. Menozzi, A. Motta, E. Otero, P. Ohresser, P. Sainctavit, G. G. Condorelli, E. Dalcanale and R. Sessoli, *Nat. Commun.*, 2014, **5**, 4582.
35. V. Corradini, A. Ghirri, E. Garlatti, R. Biagi, V. De Renzi, U. del Pennino, V. Bellini, S. Carretta, P. Santini, G. Timco, R. E. P. Winpenny and M. Affronte, *Adv. Funct. Mater.*, 2012, **22**, 3706-3713.
36. A. Ghirri, V. Corradini, C. Cervetti, A. Candini, U. del Pennino, G. Timco, R. J. Pritchard, C. A. Murny, R. E. P. Winpenny and M. Affronte, *Adv. Funct. Mater.*, 2010, **20**, 1552-1560.
37. V. E. Campbell, M. Tonelli, I. Cimatti, J. B. Moussy, L. Torteck, Y. J. Dappe, E. Riviere, R. Guillot, S. Delprat, R. Mattana, P. Seneor, P. Ohresser, F. Choueikani, E. Otero, F. Koprowiak, V. G. Chilkuri, N. Suaud, N. Guihery, A. Galtayries, F. Miserque, M. A. Arrio, P. Sainctavit and T. Mallah, *Nat. Commun.*, 2016, **7**.
38. C. Train, G. Rikken and M. Verdaguer, in *Molecular Magnetic Materials: Concepts and Applications*, eds. B. Sieklucka and D. Pinkowicz, Wiley - VCH Verlag GmbH & Co. KGaA, 2016, ch. 11, pp. 301-322. DOI: 10.1039/C8SC04917C
39. H. D. Flack, *Helv. Chim. Acta*, 2003, **86**, 905-921.
40. B. L. Silver, *Irreducible tensor methods : an introduction for chemists*, Academic, New York, 1976.
41. E. Anderson, *LAPACK Users's Guide*, Society for Industrial and Applied Mathematics, Philadelphia, 2nd edn., 1995.
42. W. H. Press, B. P. Flannery, S. A. Teukolsky and W. T. Vetterling, *Numerical recipes : the art of scientific computing*, Cambridge University Press, Cambridge, 1992.
43. C. J. Milios, R. Inglis, A. Vinslava, R. Bagai, W. Wernsdorfer, S. Parsons, S. P. Perlepes, G. Christou and E. K. Brechin, *J. Am. Chem. Soc.*, 2007, **129**, 12505-12511.
44. R. Inglis, C. J. Milios, L. F. Jones, S. Piligkos and E. K. Brechin, *Chem. Commun.*, 2012, **48**, 181-190.
45. E. R. Davidson, *J. Comput. Phys.*, 1975, **17**, 87-94.
46. B. Liu, *Numerical Algorithms in Chemistry: Algebraic Method*, Lawrence Berkeley Laboratory, University of California, California, 1978, 49-53.
47. S. Piligkos, E. Bill, D. Collison, E. J. L. McInnes, G. A. Timco, H. Weihe, R. E. P. Winpenny and F. Neese, *J. Am. Chem. Soc.*, 2007, **129**, 760-761.
48. S. Piligkos, H. Weihe, E. Bill, F. Neese, H. El Mkami, G. M. Smith, D. Collison, G. Rajaraman, G. A. Timco, R. E. P. Winpenny and E. J. L. McInnes, *Chem.Eur. J.*, 2009, **15**, 3152-3167.
49. E. K. Fields and S. Meyerson, *Acc. Chem. Res.*, 1969, **2**, 273-&.
50. R. Inglis, J. Bendix, T. Brock-Nannestad, H. Weihe, E. K. Brechin and S. Piligkos, *Chem. Sci.*, 2010, **1**, 631-636.
51. A. R. Tomsa, J. Martinez-Lillo, Y. L. Li, L. M. Chamoreau, K. Boubekeur, F. Farias, M. A. Novak, E. Cremades, E. Ruiz, A. Proust, M. Verdaguer and P. Gouzerh, *Chem. Commun.*, 2010, **46**, 5106-5108.
52. M. Soler, W. Wernsdorfer, Z. M. Sun, J. C. Huffman, D. N. Hendrickson and G. Christou, *Chem. Commun.*, 2003, DOI: 10.1039/b306246e, 2672-2673.
53. P. Parois, S. A. Moggach, J. Sanchez-Benitez, K. V. Kamenev, A. R. Lennie, J. E. Warren, E. K. Brechin, S. Parsons and M. Murrie, *Chem. Commun.*, 2010, **46**, 1881-1883.
54. H. Hakkinen, *Nat. Chem.*, 2012, **4**, 443.
55. E. Pensa, E. Cortes, G. Corthey, P. Carro, C. Vericat, M. H. Fonticelli, G. Benitez, A. A. Rubert and R. C. Salvarezza, *Acc. Chem. Res.*, 2012, **45**, 1183-1192.
56. M. Perfetti, F. Pineider, L. Poggini, E. Otero, M. Mannini, L. Sorace, C. Sangregorio, A. Cornia and R. Sessoli, *Small*, 2014, **10**, 323-329.
57. I. Ashur, O. Schulz, C. L. McIntosh, I. Pinkas, R. Ros and A. K. Jones, *Langmuir*, 2012, **28**, 5861-5871.
58. R. Bukasov and J. S. Shumaker-Parry, *Nano Lett.*, 2007, **7**, 1113-1118.
59. D. G. Castner, K. Hinds and D. W. Grainger, *Langmuir*, 1996, **12**, 5083-5086.
60. T. M. Willey, A. L. Vance, C. Bostedt, T. van Buuren, R. W. Meulenberg, L. J. Terminello and C. S. Fadley, *Langmuir*, 2004, **20**, 4939-4944.
61. J. Dreiser, A. M. Ako, C. Wackerlin, J. Heidler, C. E. Anson, A. K. Powell, C. Piamonteze, F. Nolting, S. Rusponi and H. Brune, *The Journal of Physical Chemistry C*, 2015, **119**, 3550-3555.



62. M. Shima, K. Tsutsumi, A. Tanaka, H. Onodera and M. Tanemura, *Surf. Interface Anal.*, 2018, **50**, 1187-1190.
63. M. C. Biesinger, L. W. M. Lau, A. R. Gerson and R. S. C. Smart, *Phys. Chem. Chem. Phys.*, 2012, **14**, 2434-2442.
64. S. A. Pizarro, P. Glatzel, H. Visser, J. H. Robblee, G. Christou, U. Bergmann and V. K. Yachandra, *Phys. Chem. Chem. Phys.*, 2004, **6**, 4864-4870.
65. S. Wang, L. Kong, H. Yang, Z. He, Z. Jiang, D. Li, S. Zeng, M. Niu, Y. Song and J. Dou, *Inorg. Chem.*, 2011, **50**, 2705-2707.
66. N. Kawamura, T. Yamamoto, H. Maruyama, I. Harada, M. Suzuki and T. Ishikawa, *Journal of Synchrotron Radiation*, 2001, **8**, 410-412.
67. E. Sarigiannidou, F. Wilhelm, E. Monroy, R. M. Galera, E. Bellet-Amalric, A. Rogalev, J. Goulon, J. Cibert and H. Mariette, *Phys. Rev. B*, 2006, **74**.
68. G. L. Nealon, B. Donnio, R. Greget, J.-P. Kappler, E. Terazzi and J.-L. Gallani, *Nanoscale*, 2012, **4**, 5244-5258.
69. I. Carmeli, G. Leitus, R. Naaman, S. Reich and Z. Vager, *The Journal of Chemical Physics*, 2003, **118**, 10372-10375.
70. P. Crespo, R. Litrán, T. C. Rojas, M. Multigner, J. M. de la Fuente, J. C. Sánchez-López, M. A. García, A. Hernando, S. Penadés and A. Fernández, *Phys. Rev. Lett.*, 2004, **93**, 087204.
71. S. Trudel, *Gold Bull.*, 2011, **44**, 3-13.
72. R. Singh, *J. Magn. Magn. Mater.*, 2013, **346**, 58-73.
73. F. Tassinari, D. R. Jayarathna, N. Kantor-Uriel, K. L. Davis, V. Varade, C. Achim and R. Naaman, *Adv. Mater. (Weinheim, Ger.)*, 2018, **30**, 1706423.
74. H. Al-Bustami, G. Koplovitz, D. Primc, S. Yochelis, E. Capua, D. Porath, R. Naaman and Y. Paltiel, *Small*, 2018, **14**, 1801249.
75. J. S. Garitaonandia, M. Insausti, E. Goikolea, M. Suzuki, J. D. Cashion, N. Kawamura, H. Ohsawa, I. Gil de Muro, K. Suzuki, F. Plazaola and T. Rojo, *Nano Lett.*, 2008, **8**, 661-667.
76. J. Dreiser, G. E. Pacchioni, F. Donati, L. Gragnaniello, A. Cavallin, K. S. Pedersen, J. Bendix, B. Delley, M. Pivetta, S. Rusponi and H. Brune, *ACS Nano*, 2016, **10**, 2887-2892.

View Article Online
DOI: 10.1039/C8SC04917C



